Computational indentation in highly cross-linked polymer networks

Manoj Kumar Maurya [1], Céline Ruscher [2], Debashish Mukherji [3,*] and Manjesh Kumar Singh [1,†]

[1]*Department of Mechanical Engineering, Indian Institute of Technology Kanpur, Kanpur UP 208016, India*
[2]*Department of Mechanical Engineering, University of British Columbia, Vancouver, Canada BC V6T 1Z4*
[3]*Quantum Matter Institute, University of British Columbia, Vancouver, Canada BC V6T 1Z4*

Indentation is a common experimental technique to study the mechanics of polymeric materials. The main advantage of using indentation is this provides a direct correlation between the microstructure and the small-scale mechanical response, which is otherwise difficult within the standard tensile testing. The majority of studies have investigated hydrogels, microgels, elastomers, and even soft biomaterials. However, a less investigated system is the indentation in highly cross-linked polymer (HCP) networks, where the complex network structure plays a key role in dictating their physical properties. In this work, we investigate the structure-property relationship in HCP networks using the computational indentation of a generic model. We establish a correlation between the local bond breaking, network rearrangement, and small-scale mechanics. The results are compared with the elastic-plastic deformation model. HCPs harden upon indentation.

I. INTRODUCTION

Polymers are ubiquitous since the early start of life in the form of natural rubber, starch, and cellulose [1–4]. However, the concept of synthetic polymers is relatively new, which was first proposed in the pioneering work of Staudinger [5]. Polymers are of particular interest because the relevant energy scale in these materials is about $k_B T$ at the ambient temperature, thus their properties are dictated by the large conformational and compositional fluctuations [6–9]. Here k_B is the Boltzmann constant. Therefore, polymers provide a suitable platform for the flexible design of advanced soft materials. For example, polymers are widely used for lubrication [10–13], confinement mechanics of biological materials [14–17], smart materials [8,18,19], thermoelectrics [20,21], and common daily-use materials [22–25], to name a few.

Traditionally linear polymers are commonly used for various applications [6–8,22], while more recent interests have been directed towards the cross-linked polymers that range from elastomers (weakly cross-linked) to epoxies (highly cross-linked) [26–28]. Cross-linked, in particular highly cross-lined polymers (HCP), are important because they are light-weight, high-strength materials that can also have self-healing properties [29–32]. Here one of the important physical properties of HCPs, and polymers in general, is their mechanical response [26–28]. Therefore, a more in-depth understanding of the mechanics is needed for the advanced applications of polymeric materials with tunable properties.

Experimentally, two of the most common techniques are the tensile (or shear) deformation [29,30,33,34] and the nano-indentation [35–40]. The former technique has been extensively employed in the standard experimental setups [28–30] and in a variety of computational studies [26,27], which gives the bulk mechanics. However, within the tensile studies, the localized force response due to the small-scale complex structures becomes exceedingly difficult to extract. In this context, mechanical indentation may serve as a better technique, where extensive recent experimental efforts have been performed [35,36,41], while computational indentation studies in polymers are rather limited [42]. Additionally, indentation experiments are used to measure the hardness of materials and have the basic goal of quantifying materials' resistance to plastic deformation.

Indentation-based techniques have been extensively employed for the polymeric systems, such as hydrogels, microgels, and elastomers [37,38,43] and often used to measure the mechanical stiffness in the biological cells [44,45]. Moreover, similar studies in HCP are limited. Here, using large-scale molecular dynamics simulations of a generic model, we have studied the mechanics of HCP networks with different functionalities using computational indentation. To the best of our knowledge, until now the computational works have "only" employed the tensile deformation for polymers [46–51], and the indentation simulations are usually performed on the crystalline nanostructures [52]. Therefore, the investigation discussed herein is an attempt that employs the indentation technique for HCPs within a generic mesoscale framework.

We note in passing that for this study we have employed a (chemically independent) generic model. While generic models are extremely useful to make qualitative comparisons with the experiments, they do not provide any quantitative agreement with a chemical specific system. Moreover, for the HCP networks, very little experimental information is known regarding the network microstructures, and thus even an all-atom representation of HCP does not guarantee any realistic case known from a native chemical system. Therefore, we

*debashish.mukherji@ubc.ca
†manjesh@iitk.ac.in

have deliberately chosen to use generic model where tuning the system parameters for the desired property is rather trivial.

The remainder of the paper is organized as follows: In Sec. II we sketch our methodology. Results and discussions are presented in Sec. III, and finally, the conclusions are drawn in Sec. IV.

II. MODEL AND METHOD

HCP networks with two different network functionalities n are chosen for this study. Here n defines the maximum number of bonds that a monomer can form with its neighboring monomers. We have chosen a system of trifunctional ($n = 3$) and a tetrafunctional ($n = 4$) networks. The systems consist of $N = 2.53 \times 10^5$ Lennard-Jones (LJ) particles randomly distributed within a cubic box at an initial monomer number density $\rho_m = 0.85\sigma^{-3}$. The simulations are performed using the LAMMPS molecular dynamics package [53].

A. Interaction potentials

We employ a generic molecular dynamics simulation approach. Here the nonbonded monomers interact with a 6–12 LJ potential $u_{nb}(r) = 4\epsilon[(\sigma/r)^{12} - (\sigma/r)^6] - u_{cut}$ if the distance r between two monomers is less than a cutoff distance $r_c = 2.5\sigma$. $u_{nonbonded}(r) = 0$ for $r > r_c$, and u_{cut} is chosen such that the potential is continuous at r_c. Here ϵ and σ are the LJ energy and the LJ length, respectively. This leads to a unit of time $\tau = \sigma\sqrt{m/\epsilon}$, with m being the mass of the monomers. The unit of force F is ϵ/σ. The values representative of the hydrocarbons are $\epsilon = 30$ meV, $\sigma = 0.5$ nm, and $\tau = 3$ ps. The unit of pressure $P_\circ = 40$ MPa [54].

The equations of motion are integrated using the velocity Verlet algorithm with a time step 0.005τ, and the temperature is set to $T = 1\epsilon/k_B$, which is much higher than the typical glass transition temperature $T_g \simeq 0.4\epsilon/k_B$ in these networks [26,27], thus representing a HCP gel phase. The temperature is imposed using a Langevin thermostat with a damping coefficient of $\gamma = 1\tau^{-1}$. The initial LJ system is equilibrated for 5×10^5 steps.

To model the HCP networks, we have used two different bonded interactions $u_b(r)$: the finitely extensible nonlinear elastic (FENE) [54] and the quartic potential [26,55].

B. Network cure

During the network formation FENE is used, where a bond between two monomers is defined by the combination of the repulsive 6–12 LJ potential,

$$u_b(r) = 4\epsilon\left[\left(\frac{\sigma}{r}\right)^{12} - \left(\frac{\sigma}{r}\right)^6 + \frac{1}{4}\right] \text{ for } r < 2^{1/6}\sigma_b, \quad (1)$$

and the FENE potential,

$$u_{FENE}(r) = -\frac{1}{2}kR_\circ^2 \ln\left[1 - \left(\frac{r}{R_\circ}\right)^2\right]. \quad (2)$$

Here $k = 30k_BT/\sigma^2$ and $R_\circ = 1.5\sigma$. This gives a typical bond length of $\ell_b \simeq 0.97\sigma$ [54]; see the black curve in Fig. 1.

Because the indentation is performed along the z direction, the starting configuration (before curing) consists of a homogeneous sample of LJ particles at ρ_m confined between two
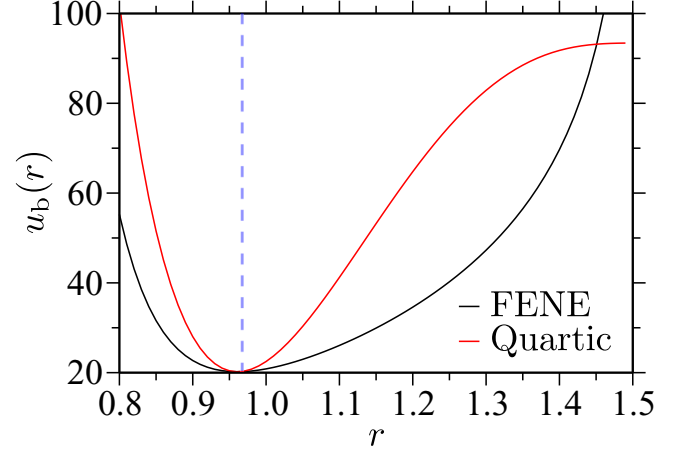

FIG. 1. Interaction potentials between the bonded monomers $u_b(r)$ as a function of intermonomer distance r. The quartic parameters are taken from the literature [55]. The equilibrium bond length for these models is around $\ell_b = 0.97\sigma$ represented by the vertical line.

repulsive walls along the z direction. The periodic boundary conditions are employed in the x and the y directions. The bonds are allowed to form between the monomers using a protocol proposed in some of our earlier works [56,57]. Within this protocol, the bonds are randomly formed between two monomers when (1) two particles are closer than 1.1σ distance, (2) monomers have not formed the maximum number of possible bonds limited by n, and (3) a random number between zero and one is less than the bond forming probability of 0.05. The network curing is performed for $t_{cure} = 5 \times 10^3\tau$ during the canonical simulation. Here t_{cure} is sufficient to attain close to 99% cure; see Fig. 2. This procedure also ensures
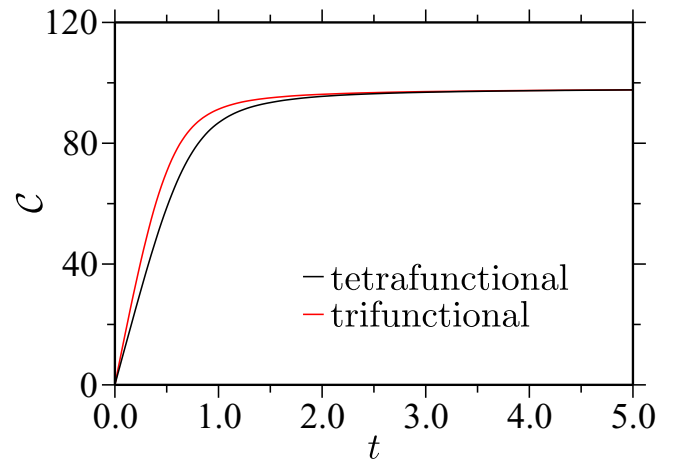

FIG. 2. Curing percentages C during the formation of total number of bonds $\mathcal{N}_b$ with time t for two network functionalities n. The data are shown for the trifunctional ($n = 3$) and the tetrafunctional ($n = 4$) systems. Network cure is performed via FENE bonds; see Eq. (2). Note that for the representation purpose we have shown results only for the initial time of 5τ, while the total simulation time is $5 \times 10^3\tau$.

a rather homogeneous bond formations within the sample; see Fig. 8 in Appendix A.

After the network curing stage, systems are equilibrated for $t_{\mathrm{NPT}} = 2.55 \times 10^3 \tau$ at zero pressure. Here pressure is employed using a Nose-Hoover barostat with pressure-damping parameter $\gamma_{\mathrm{p}} = 0.5\tau$.

C. Computational indentation

For the indentation simulations, we have used a quartic potential [55],

$$u_{\mathrm{quartic}}(r) = k\tilde{r}^2(\tilde{r} - B_1)(\tilde{r} - B_2) + u_\circ. \tag{3}$$

Here $k = 2351k_{\mathrm{B}}T/\sigma^4$, $\tilde{r} = r - R_c$, $R_c = 1.5\sigma$, $B_1 = 0$, $B_2 = -0.7425\sigma$, and $u_\circ = 92.744k_{\mathrm{B}}T$. This potential ensures bond breaking if the distance between two bonded monomers is larger than R_c.

An implicit spherical indenter of radius R is used. The force acting on the indenter is obtained by summing the force contributions of the first shell surrounding monomers. Here the individual force is calculated using the derivative of $u_{\mathrm{indenter}}(r) = K(r - R)^2$, where $K = 100\,k_{\mathrm{B}}T/\sigma^2$ is the force constant and r is the distance from the atom to the center of the indenter. The indentation is performed at a constant velocity $v = 0.005\sigma/\tau$ and in the microcanonical ensemble. Two indenters with $R = 5.0\sigma$ and 15.0σ are chosen for this work.

We note in passing that we have also conducted simulations at $v = 0.05\sigma/\tau$. The results showed no noticeable difference for the tetrafunctional sample, while a significant difference was observed for the trifunctional system (data not shown). Therefore, we have chosen $v = 0.005\sigma/\tau$ below which the mechanical response remains invariant irrespective of the network functionality. To test the reproducibility of the data, we have performed three sets of simulations for $R = 5.0\sigma$ and for both functionalities. The data are shown by Fig. 13 in Appendix F.

III. RESULTS AND DISCUSSION

A. Force response upon indentation

We start by discussing the mechanical response of a tetrafunctional HCP network. Figure 3 shows the typical force F versus indentation d behavior for two different R. Other than the generic behavior, i.e., the increase in F with increasing d, one interesting feature that can be seen is the sudden force drop ΔF at various d. Note that we define ΔF only when its magnitude is larger than the percentage of error fluctuation calculated in the elastic regime, i.e., below bond breaking indicated by the black arrows in Fig. 3. Such a force drop is a well-known phenomenon in the mechanical response of the glassy materials, where the atomic rearrangements during deformation can lead to such force drops [58]. This phenomenon is commonly referred to as the *avalanche*. In our study, however, we are dealing with a rather rigid cross-linked network that has microscopically different molecular connectivity in comparison to the common glasses.

What causes such avalanche-like deformation in HCP? To investigate this issue, we have calculated the percentage of bond breaking $\mathcal{B}$ as a function of d. It can be appreciated
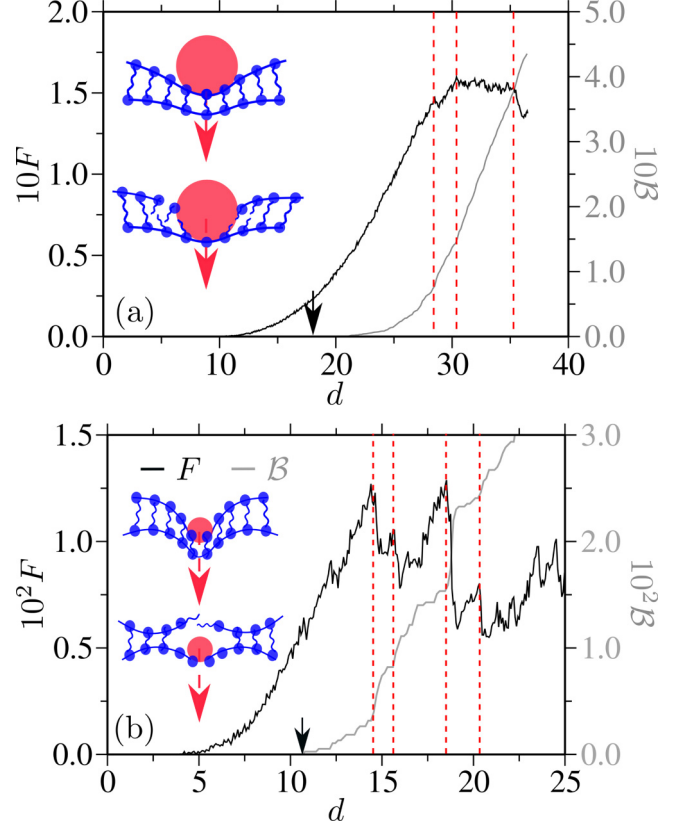

FIG. 3. Force F and the percentage of broken bonds $\mathcal{B}$ as a function of the indentation depth d. (a, b) Data for the indenter radius $R = 15.0\sigma$ (a) and 5.0σ (b). The color codes of the data sets are consistent with their corresponding y axes. Data are shown for an indentation velocity of $0.005\sigma/\tau$ and for a tetrafunctional network. Vertical lines highlight the major drops in F and the corresponding $\mathcal{B}$. Initial depletion zones below $d < 10.0\sigma$ (a) and $d < 5.0\sigma$ (b) are because the lowest part of the indentation tips are certain distance away from the network surface. Arrow indicates at the d values where the bond breaking starts. The insets show different pictorial representations of the indentation tips entering the sample at different d. The top and the bottom panels show the cases just before and after the bond breaking in the samples, respectively.

that ΔF (see the black data sets in Fig. 3) is directly related to the large number of broken bonds (see the light gray data sets in Fig. 3). This behavior is quite expected because the strongly interacting bonded monomers can significantly resist the deformation. When the bonds break, they induce large force drops in HCPs. In the insets of Fig. 3 we show the possible pictorial representations of the cases just before and after the bond breaking in these samples. Such avalanches, induced by the bond breaking, were also observed in a combined experimental and simulation study on soft polymer networks [42].

Figure 3 also reveals that ΔF is more prominent for $R = 5.0\sigma$ in comparison to $R = 15.0\sigma$. This behavior is not surprising given that the smaller indenter can delicately monitor the bond breaking that occurs at the monomer level, while the larger indenter tip can monitor only a larger group of monomers that on average contribute to F and $\mathcal{B}$. We also note in passing that the standard tensile deformation can investigate
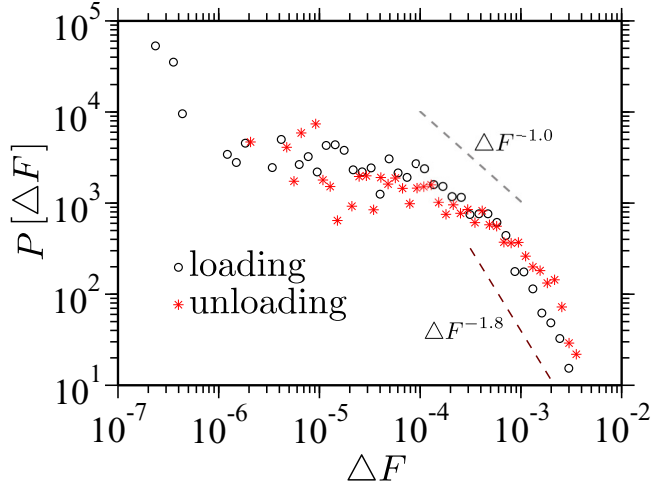
FIG. 4. Distribution of the force drops $P(\Delta F)$ obtained from Fig. 3(b). ΔF is calculated at the onset of bond breaking in the tetrafunctional networks. The data are shown for an indenter radius $R = 5\sigma$. The lines are power-law fits, $\Delta F^{-1.0}$ (for $10^{-4} < \Delta F < 10^{-3}$) and $\Delta F^{-1.8}$ (for $\Delta F > 10^{-3}$). We have also added the data corresponding to the unloading cycle. The data are averaged over three different simulation runs, as described by Fig. 13 in Appendix F.

only the bulk mechanical behavior [27], while the indentation simulations can reveal the small-scale microscopic structural details because of the localized deformation, which is also intrinsically related to R. Additionally, the relatively larger F values for $R = 15.0\sigma$ is because this indenter tip has on average a larger number of monomers that are directly in contact with it.

As discussed above, the observed trends in ΔF are reminiscent of the mechanics of amorphous materials. It would therefore be interesting to see whether the distribution of ΔF follows a scaling law as is the case for sheared amorphous systems [59]. For this purpose, we have also calculated distribution of ΔF for our systems $P(\Delta F)$. The corresponding data are shown in Fig. 4. It can be appreciated that the data show three regimes: a plateau for $\Delta F < 10^{-4}$, $P(\Delta F) \propto$

$\Delta F^{-1.0}$ for a narrow region $10^{-4} < \Delta F < 10^{-3}$, and finally $P(\Delta F) \propto \Delta F^{-1.8}$ for $\Delta F > 10^{-3}$. For the elastic-plastic deformation of glassy systems, most of the studies have focused on the distribution of avalanches in the stationary regime. In these cases, three-dimensional simulations have reported the exponents within the range of 1.2–1.3 [59,60]. However, only a few works have dealt with the transient regime, and results obtained so far suggest either a similar value of the avalanche exponent as in the stationary regime [60] or smaller [61]. In this context, the gel phase of HCP systems investigated here is microscopically different from the traditional monoatomic glass formers. Therefore, we can only point toward the relatively close value of the avalanche exponent without attempting to state precisely why this description still holds in our case. Moreover, the close resemblance of the mechanical behavior observed between two microscopically distinct systems may direct towards a more generic mechanical picture of the jammed systems. We also note in passing that the goal of this work is not to study the scaling laws of $P(\Delta F)$, rather to study only any possible close resemblance with the avalanche-like behavior. Therefore, we abstain from going into further detail on this aspect.

B. Mechanics during loading and unloading

In the typical elastomers, microgels, hydrogels, and/or polymers, the deformation is usually viscoelastic in nature upon small deformations. However, mechanical indentation in HCPs also induces a significant amount of bonds breaking and thus is expected to follow the elastic-plastic deformation. In this context, it has been previously shown that the depth sensing of the materials can be investigated within the loading-unloading setup [62]. Furthermore, the hardness, stiffness, and effective elastic modulus of a sample can be readily calculated. Therefore, in this section we investigate HCPs under cyclic loading.

Figure 5 shows the mechanics of HCPs during the loading and the unloading cycles. The significant hysteresis indicate at a large plastic deformation in the samples, resulting from a large number of the broken bonds. Furthermore, the strong
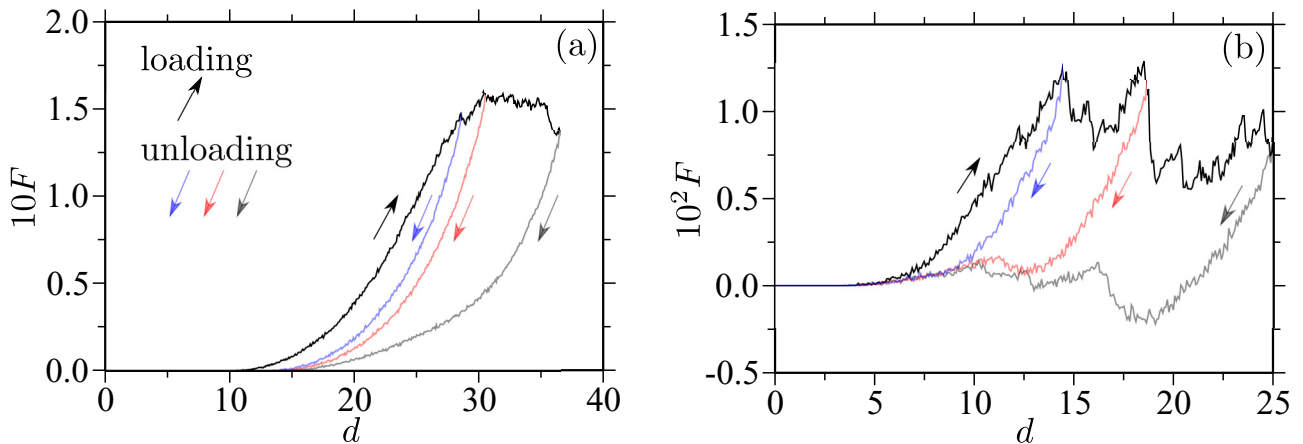

FIG. 5. Same as Fig. 3, however, during both loading and unloading cycles. Arrows indicate the corresponding loading and unloading curves. [(a), (b)] Data for the indenter radius $R = 15.0\sigma$ (a) and $R = 5.0\sigma$ (b). For clarity of presentation, we have shown only four data sets in (a). More data are presented in Fig. 9 in Appendix B.

TABLE I. Observables for the calculation of effective elastic modulus E_{eff} in Eq. 4. Data are shown for the tetrafunctional networks and for two different indenter radius R. $d_{\max}$ and $F_{\max}$ are the maximum displacement and force just before the unloading, respectively. The slope S is calculated from the initial linear regime during unloading. d_c is the contact depth between the spherical indenter and the sample, and $\mathcal{A}$ is the contact area. Note that for the calculation of $d_{\max}$, the initial depletion zones in Fig. 5 are subtracted.

$R\,[\sigma]$	$d_{\max}\,[\sigma]$	$F_{\max}\,[k_{\text{B}}T/\sigma]$	$S = \frac{dF}{dd}\,[k_{\text{B}}T/\sigma^2]$	$d_c\,[\sigma]$	$\mathcal{A}\,[\sigma^2]$	$10^2 E_{\text{eff}}\,[k_{\text{B}}T/\sigma^3]$
15.0	4.1	0.006	0.0029	2.5	215.98	17.49
	9.0	0.038	0.0087	6.5	479.88	35.20
	15.8	0.111	0.0194	11.5	668.37	66.50
	18.5	0.147	0.0226	13.6	700.70	75.66
	20.5	0.158	0.0234	15.4	706.36	78.03
	26.5	0.137	0.0204	21.5	574.13	75.45
5.0	10.4	0.013	0.0038	7.9	52.12	46.65
	14.6	0.013	0.0025	10.7	—	—
	21.0	0.008	0.0021	18.1	—	—

undershooting, $F < 0$ for $R = 5.0\sigma$, in Fig. 5(b) is because an unloading cycle pulls a certain number of monomers that induces a negative pressure in the samples. This behavior is in good agreement with a set of recent experiments on hydrogels, where large force drops during the loading cycles and strong hysteresis during the unloading cycles were observed [63]. It should also be highlighted that the most severe effects of hysteresis are observed for $d \geqslant 2R$. We will come back to this point below.

Having shown the mechanics during the loading and the unloading cycles, we will now investigate if the relevant system properties can be extracted from the data in Fig. 5. In this context, there is a theory that connects the mechanics under the unloading cycles to the material stiffness via the so-called effective elastic modulus E_{eff} [62],

$$E_{\text{eff}} = \frac{S}{2}\sqrt{\frac{\pi}{\mathcal{A}}}. \tag{4}$$

Here $S = \mathrm{d}F/\mathrm{d}d$ is calculated from the initial displacements during the unloading cycles. The contact area for a spherical indenter can be estimated using $\mathcal{A} = 2\pi R d_c - \pi d_c^2$, and the contact depth between the indenter and the sample is $d_c = d_{\max} - 0.75 F_{\max}/S$. We note in passing that this theory was initially developed for the Berkovich contact [62]. It is widely used in typical micro- and nano-indentation experiments. A more general treatment is discussed there dealt with different indenter shapes [62].

Using Eq. (4) we have calculated E_{eff} during the unloading at different indentation depths and for both R. The data are compiled in Table I. For $R = 15.0\sigma$, it can be appreciated that E_{eff} increases with increasing $d_{\max}$, before reaching a plateau at $d_{\max} > R$. This length scale is also consistent with the d value at which the force plateaus in Fig. 5.

The stiffening upon deformation is reminiscent of the strain-hardening behavior in polymeric materials [57,64]. In this context, it has been previously shown that a tetrafunctional HCP can strain-harden under tensile deformation [27]. There it was argued that the network curing protocol induces a significant amount of free volume within the cured samples. These free volumes usually collapse to form rather large protovoids centers, where the monomers around the periphery of a protovoids can statistically form bonds pointing away from each other. During the tensile deformation, these protovoids

open up by disrupting the van der Waals (vdW) contacts and thus may be a possible cause for the strain hardening. In contrast to the tensile testing, indentation compresses a sample. Such compression-induced hardening results from two effects: (1) the small-scale tension that builds up when the certain number of bonds are pulled taut, while some other are compressed, and (2) the two boundaries of a protovoid interacting via vdW forces that can plastically slide past each other. These two combined effects lead to the major contributions to the increased E_{eff}, which we name *indentation hardening*.

Equation (4) also shows that for $d_{\max} > 2R$ and $R = 5.0\sigma$, E_{eff} is not defined. This is particularly because Eq. (4) holds only for the small relative indentations, i.e., when $d_c \leqslant 2R$.

The theoretical treatment described above does not account for the dynamics, such as the systems exhibiting viscoelastic deformation. Here one may expect the force relaxation to be significantly faster than the structural relaxation. On the contrary, a HCP network is microscopically different, where the system shows a elastic-plastic deformation via bond breaking during the indentation; see Fig. 5. Furthermore, we find that the relaxation of F is significantly slower than the structural relaxation; see Fig. 10 in Appendix C.

We also wish to highlight that the HCP networks investigated here are in their gel phase where the high-frequency elastic contacts due to the chain connectivity in the network architectures play the crucial role in restoring the network structures. The mode of this temporal relaxation is shown in Fig. 10 in Appendix C.

C. Effect of network functionality

The network functionality n is also expected to significantly impact the force response. For this purpose, here we show the system with $R = 5.0\sigma$ where the most prominent force drops are observed [see Fig. 3(b)] while the data for $R = 15.0\sigma$ are presented in Fig. 11 in Appendix D.

Figure 6 shows the effect of n on the mechanical response. It can be appreciated that the trifunctional system can withstand an almost twice larger indentation depth before the bond breaking happens in a sample. For example, bond breaking starts at $d \simeq 11.0\sigma$ for a tetrafunctional sample [see Fig. 3(b)], while it is about $d \simeq 21.0\sigma$ for a trifunctional system (see the inset in Fig. 6). This is particularly because the
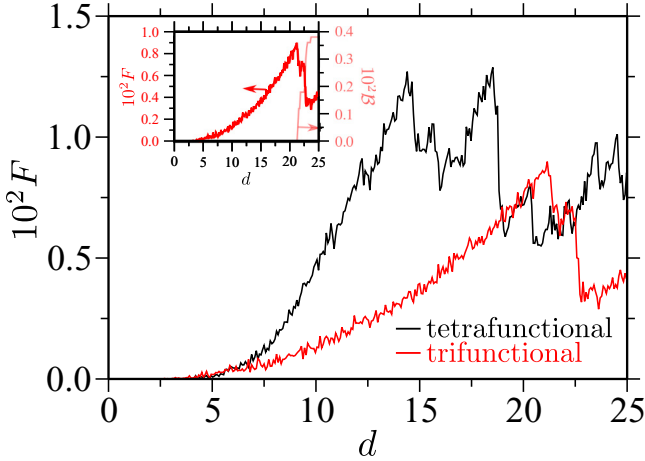
FIG. 6. Same as Fig. 3(b), but for two different network functionalities. The inset also includes the percentage of bond breaking $\mathcal{B}$ for the trifunctional network. For this network, bond breaking starts at around a depth of $d \simeq 21.0\sigma$. Data are shown for an indenter radius $R = 5.0\sigma$.

lower bond density of a trifunctional sample, in comparison to a tetrafunctional sample, can withstand a larger elastic deformation. Furthermore, a trifunctional system is twice as ductile as a tetrafunctional sample, while the maximum force these samples can withstand also reduces by about a factor of two for the former (see the main panel in Fig. 6). These results are reasonably consistent with the HCPs under the tensile deformations [57].

D. Effect of network curing percentage

One of the most important features of the HCP networks is that their mechanics can be tuned almost *at will* by tuning the amount of cure in the sample. Therefore, in this section we aim to investigate the effect of curing on the mechanics of
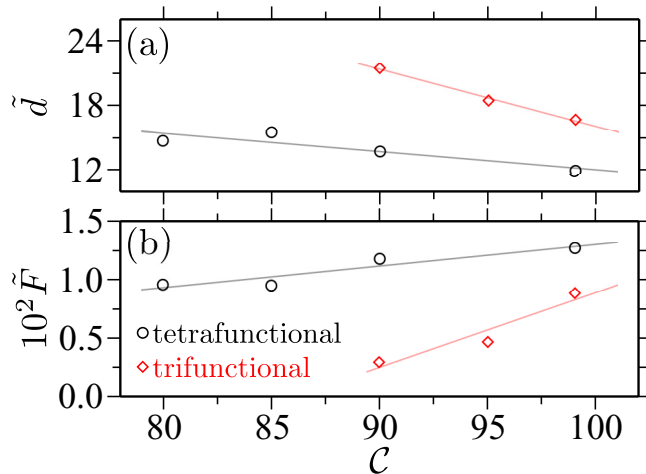

FIG. 7. The first maximum at the force drop $\tilde{F}$ and corresponding depth $\tilde{d}$ as a function of the percentage of the network cure $\mathcal{C}$. The data are shown for two different network functionalities and for an indenter radius $R = 5.0\sigma$. Note that for the calculation of $\tilde{d}$, the initial depletion zones in the force-extension curves are subtracted.

the samples. For this purpose, we have calculated the force-indentation behavior for a different percentage of cure $\mathcal{C}$; see below. From these data sets, we extract the force at the first maximum drop $\tilde{F}$ and the corresponding indentation depth $\tilde{d}$. Figure 7 shows the variation of $\tilde{F}$ and $\tilde{d}$ with the change in $\mathcal{C}$. The data clearly indicate a reasonable linear variation that can serve as a guiding tool for the possible synthesis of epoxies with tunable mechanical response.

IV. CONCLUSION AND DISCUSSION

Using large-scale molecular dynamics simulations of a (mesoscopic) generic model, we investigate the mechanical response of a set of highly cross-linked polymer (HCP) networks. For this purpose, we have used the mechanical indentation of different indenter sizes. The use of such a method has many advantages over the routinely used tensile deformations. For example, the deformations at the monomer level can be monitored because the individual bond breaking and network (re-)arrangements are directly accessible. Contrary to the viscoelastic deformations in the standard polymers, the deformations in the HCPs are of an elastic-plastic nature. An analysis based on a simple theory of elastic-plastic deformation [62] suggests that the HCP networks harden upon indentation. This is because of the bonds that are pulled or compressed taut and the disruption of the protovoids (collapsed free volume area) that originate within the sample during the network cure [56].

The results also indicate at a very intriguing force drop ΔF like mechanical response, reminiscent of the avalanche in the glassy materials. Such ΔF behavior in HCPs is related to the instantaneous bond breaking, small-scale monomeric rearrangements, and localized force response within the samples. We further show that the distribution of ΔF follows a scaling law decay with an exponent close to the theoretical predictions for the avalanches in the standard glasses.

The results presented in this work are based on a generic molecular dynamics approach that combines a broad range of chemical systems within one physical framework. While such models are extremely useful in studying the trends observed in the chemical specific systems, they do not provide any quantitative agreement with the experiments. Also note that there are generic models that are specifically tuned to reproduce certain quantities and their respective behavior [65]. Therefore, it is important to discuss the possible chemical systems that represent the HCP networks discussed here. In this context, in a generic model, one bead corresponds to a certain number of atomistic monomers [26,54], while the degree of such coarse graining is controlled by the bond and bending stiffnesses.

The experimental syntheses of HCPs, such as the epoxies, are performed with different underlying chemistry. For example, the most commonly used systems include, but are not limited to, the amine-cured epoxies [30] and the phenylenediamine-based cross-linking of a network structure [66]. These systems are rather rigid network materials that exhibit extraordinary mechanical [27,30] and thermal properties [28,56]. Furthermore, more complex structures are also synthesized that use the alkane chains for cross-linking [28]. The longer the length of the alkanes, the softer the network at

a given temperature [28]. In this context, the quartic potential parameters used in this work closely mimics the amine-based epoxies, while the FENE bonds mimic the relatively softer bonded interactions induced by the alkane-based linkers. A more detailed discussion of the atomistic to generic mapping schemes is presented in Ref. [56].

It is also important to discuss that the mechanical testing on weakly cross-linked systems, such as the PAM-based hydrogels [38], surface-grafted gels [37], and PNIPAM-based microgels [41], often leads to unexpected behavior. One of the interesting aspects of these systems is that they exhibit depth-dependent force response, i.e., the stiffness of the samples changes with the depth. This is practically because of the synthesis protocols that unavoidably introduce a greater degree of bond density at the core and decrease radially outward from the centers. In this context, while our trifunctional system may mimic such weakly cross-linked networks, the bond density in our systems is rather homogeneous across the sample; see Fig. 8. Therefore, a more careful modeling will require an additional control parameter of the nonhomogeneous bond density within the samples that can serve as a guiding tool for the materials design. A detailed discussion of this aspect will be presented elsewhere.
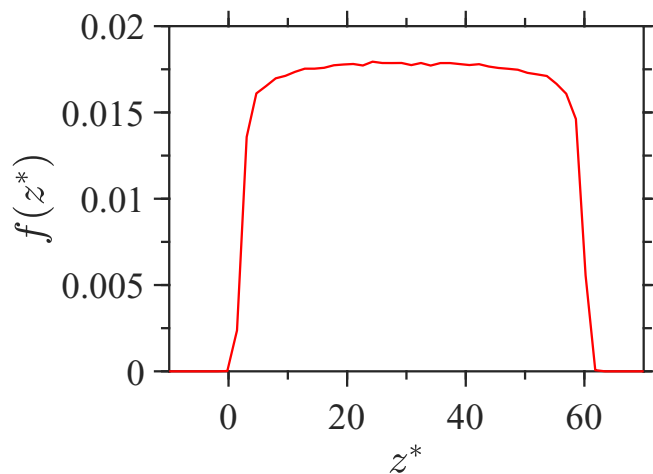
ACKNOWLEDGMENTS

FIG. 8. Bond density $f(z^*)$ along the z direction of the sample, i.e., the direction along which the indentation is applied. The data are shown for a tetrafunctional network.
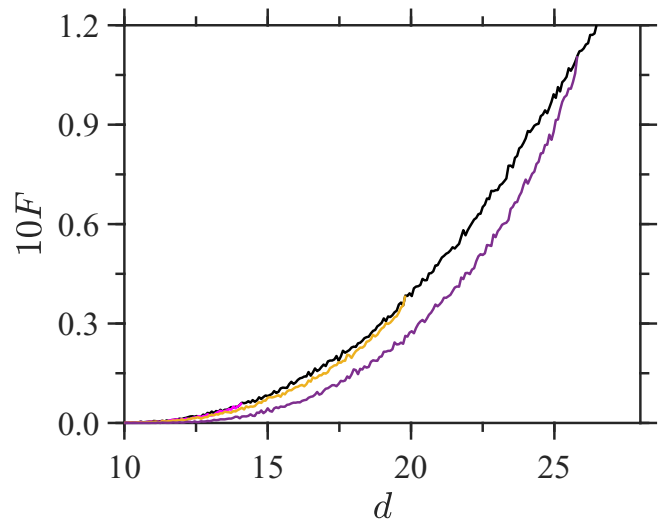

FIG. 9. Force F as a function indentation depth d during three different unloading cycles starting at different d. Data are shown for the tetrafunctional network and for an indenter radius $R = 15.0\sigma$. The unloading is performed at a constant unloading velocity $v = 0.005\sigma/\tau$. During the loading cycle, bond breaking starts only around $d \simeq 18.0\sigma$. Therefore, the unloading data starting at $d \simeq 14.0\sigma$ represent the elastic deformation. Note the data here are an extension of those in Fig. 5(a).

APPENDIX A: BOND DENSITY PROFILE

The network curing protocol presented in Sec. II B reasonably creates a homogeneous sample; see Fig. 8.

It can be appreciated that the bonds are rather homogeneous, except near the two interfaces where the confining walls induce the depletion zone.

APPENDIX B: MECHANICS DURING LOADING AND UNLOADING

In Fig. 5(a) we have shown only the force F response during unloading starting from tree indentation depths d. Here we show three additional unloading curves; see Fig. 9.

APPENDIX C: FORCE AND STRUCTURAL RELAXATIONS

To monitor the transient relaxations in a system, we have calculated the time evolution of F and the structure as monitored by d. To estimate the relaxations, we have performed two simulations. In the first case, we indent a sample using a velocity $v = 0.05\sigma/\tau$ till the maximum in the force is reached. At this position, the indenter position is fixed, and the time evolution of F is monitored. For the relaxation of d, we first decouple the indenter from a system and then monitor d with time. The data are shown in Fig. 10.

It can be appreciated that the structural relaxation is about two orders of magnitude faster than the F relaxation. At first glance this may look rather counterintuitive because the standard understanding of the dynamic systems, such as the viscoelastic deformation, suggests that the structures relax
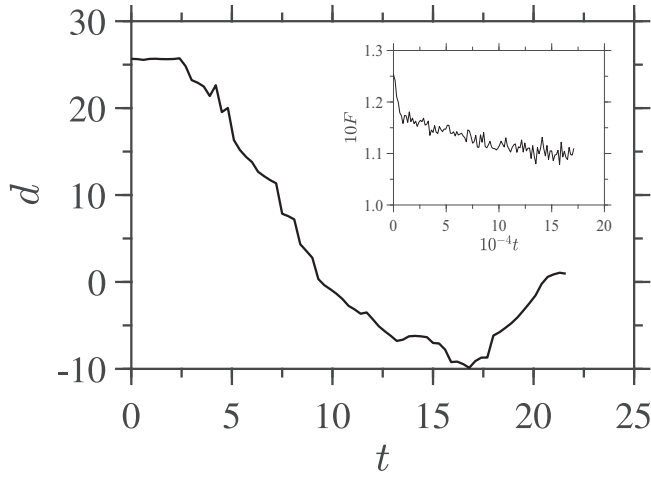
FIG. 10. Main panel shows the temporal relaxations of the depth d, and the inset presents relaxation of force F. The data are shown for the indenter radius $R = 15.0\sigma$ and for a tetrafunctional network.

significantly slower than the force. Here, however, we observe an opposite trend because we are dealing with an elastic-plastic deformation of a highly cross-linked (HCP) network structure. Furthermore, the HCP network is in its soft gel phase, where a strong restoring force acts via the bonded interactions leading to the faster structural relaxation.

APPENDIX D: EFFECT OF NETWORK FUNCTIONALITY

In Fig. 6 we have shown the comparative data of two functionalities with an indenter radius $R = 5.0\sigma$. This is particularly because the small indenter can monitor individual bond-breaking events. However, we have also calculated the mechanics of both networks using the larger indenter, i.e., for $R = 15.0\sigma$. The corresponding data are shown in Fig. 11. The data are consistent with the generic behavior discussed in
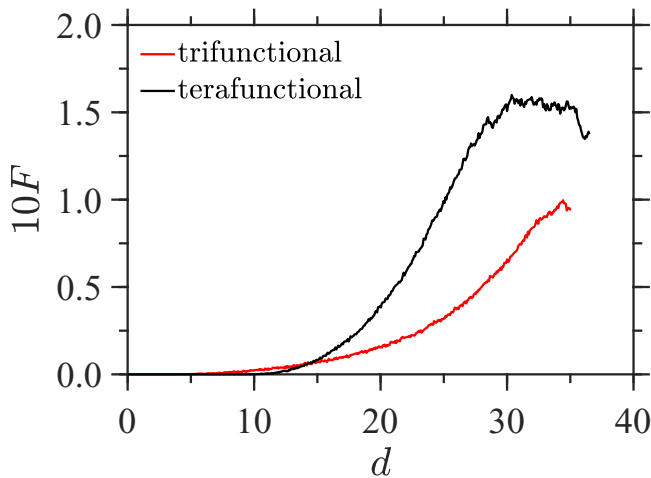

FIG. 11. Force F as a function indentation depth d for two network functionalities: the trifunctional ($n = 3$) and the tetrafunctional ($n = 4$) networks. Data are shown for an indenter radius $R = 15.0\sigma$. The indentation is performed at a constant velocity $v = 0.005\sigma/\tau$.
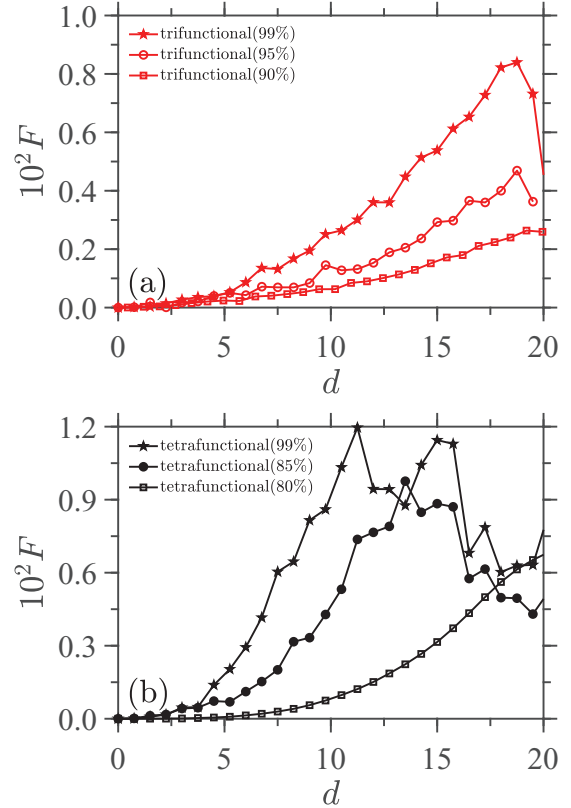

FIG. 12. Force F as a function indentation depth d for two network functionalities: the trifunctional (a) and the tetrafunctional (b) networks. Data are shown for three curing percentages $\mathcal{C}$. Note that for the clarity of presentation, we have shown only the smoothed data.

Fig. 6. Here, however, force drop events are even less prominent for the trifunctional compared to the data for $R = 5.0\sigma$; see the red lines in Fig. 6.

APPENDIX E: EFFECT OF NETWORK CURING PERCENTAGE

As shown in Fig. 7, the network curing percentage $\mathcal{C}$ plays a key role in dictating the predictive mechanical behavior that can serve as an additional tuning parameter. Note that Fig. 7 shows the extracted data from the F versus d curves at different $\mathcal{C}$; see Fig. 12.

APPENDIX F: REPRODUCIBILITY OF FORCE-INDENTATION DATA

Most studies of mechanical behavior of polymers are performed within the midsized simulation domains that many times induce large error bars. Even when our system sizes are reasonably large consisting of more than 2.5×10^5 particles, we have also performed a set of three simulations to check if the data are reproduced within the small error. In Fig. 13 the force-indentation curves for $R = 5.0\sigma$ and for both systems are shown. It can be seen that the data are reproduced within 5% error. The error bars for $R = 15.0\sigma$ are even smaller, i.e., about 1% (data not shown).
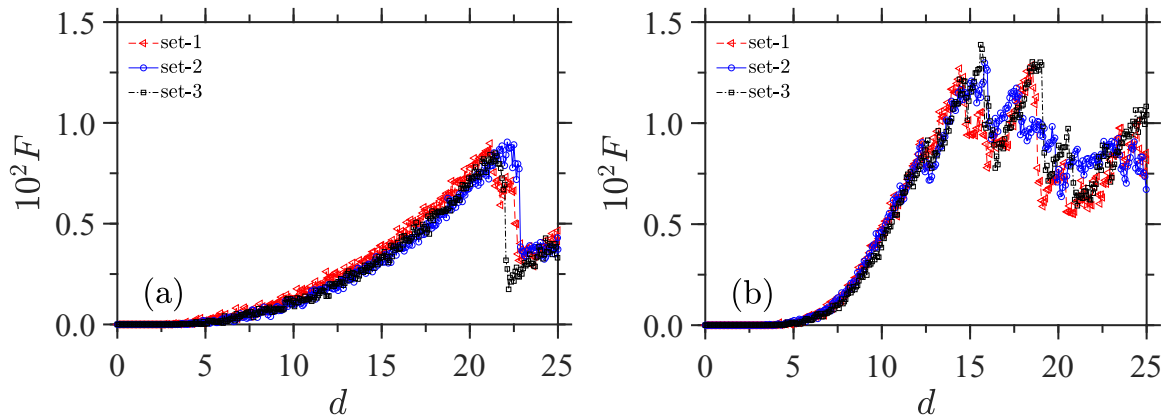
FIG. 13. Force F as a function indentation depth d for the trifunctional (a) and the tetrafunctional (b) networks. Data are shown for an indenter radius $R = 5.0\sigma$ and for three sets. The indentation is performed at a constant velocity $v = 0.005\sigma/\tau$.

[1] J. Fang, P. Fowler, C. Escrig, R. Gonzalez, J. Costa, and L. Chamudis, Development of biodegradable laminate films derived from naturally occurring carbohydrate polymers, Carbohydrate Polymers **60**, 39 (2005).

[2] D. N.-S. Hon, Cellulose and its derivatives: Structures, reactions, and medical uses, in *Polysaccharides in Medicinal Applications*, edited by Severian Dumitriu (Routledge, New York, 2017), pp. 87–105.

[3] L. Chen, X. Li, L. Li, and S. Guo, Acetylated starch-based biodegradable materials with potential biomedical applications as drug delivery systems, Curr. Appl. Phys. **7**, e90 (2007).

[4] H. M. James and E. Guth, Theory of the elastic properties of rubber, J. Chem. Phys. **11**, 455 (1943).

[5] H. Staudinger, Uber Polymerisation, Eur. J. Inorg. Chem. **53**, 1073 (1920).

[6] M. Kröger, Simple models for complex nonequilibrium fluids, Phys. Rep. **390**, 453 (2004).

[7] M. Müller, Process-directed self-assembly of copolymers: Results of and challenges for simulation studies, Prog. Polym. Sci. **101**, 101198 (2020).

[8] D. Mukherji, C. M. Marques, and K. Kremer, Smart responsive polymers: Fundamentals and design principles, Annu. Rev. Condens. Matter Phys. **11**, 271 (2020).

[9] M. K. Singh, M. Hu, Y. Cang, H.-P. Hsu, H. Therien-Aubin, K. Koynov, G. Fytas, K. Landfester, and K. Kremer, Glass transition of disentangled and entangled polymer melts: Single-chain-nanoparticles approach, Macromolecules **53**, 7312 (2020).

[10] J. Klein, E. Kumacheva, D. Mahalu, D. Perahia, and L. J. Fetters, Reduction of frictional forces between solid surfaces bearing polymer brushes, Nature (London) **370**, 634 (1994).

[11] S. de Beer, E. Kutnyanszky, P. M. Schön, G. J. Vancso, and M. H. Müser, Solvent-induced immiscibility of polymer brushes eliminates dissipation channels, Nat. Commun. **5**, 3781 (2014).

[12] M. K. Singh, P. Ilg, R. M. Espinosa-Marzal, M. Kröger, and N. D. Spencer, Polymer brushes under shear: Molecular dynamics simulations compared to experiments, Langmuir **31**, 4798 (2015).

[13] M. K. Singh, Polymer brush based tribology, *in Tribology in Materials and Applications*, edited by J. Katiyar, P. Ramkumar, T. Rao, and J. Davim, Materials Forming, Machining and Tribology (Springer, Cham, 2020), pp. 15–32.

[14] D. Missirlis and J. P. Spatz, Combined effects of peg hydrogel elasticity and cell-adhesive coating on fibroblast adhesion and persistent migration, Biomacromolecules **15**, 195 (2014).

[15] S. H. Kim, A. Opdahl, C. Marmo, and G. A. Somorjai, AFM and SFG studies of PHEMA-based hydrogel contact lens surfaces in saline solution: Adhesion, friction, and the presence of non-crosslinked polymer chains at the surface, Biomaterials **23**, 1657 (2002).

[16] J. H. Wen, L. G. Vincent, A. Fuhrmann, Y. S. Choi, K. C. Hribar, H. Taylor-Weiner, S. Chen, and A. J. Engler, Interplay of matrix stiffness and protein tethering in stem cell differentiation, Nat. Mater. **13**, 979 (2014).

[17] J. A. Beamish, J. Zhu, K. Kottke-Marchant, and R. E. Marchant, The effects of monoacrylated poly (ethylene glycol) on the properties of poly (ethylene glycol) diacrylate hydrogels used for tissue engineering, J. Biomed. Mater. Res. A **92A**, 441 (2010).

[18] R. Brighenti, Y. Li, and F. J. Vernerey, Smart polymers for advanced applications: A mechanical perspective review, Front. Mater. **7**, 196 (2020).

[19] M. A. C. Stuart, W. T. Huck, J. Genzer, M. Müller, C. Ober, M. Stamm, G. B. Sukhorukov, I. Szleifer, V. V. Tsukruk, and M. Urban *et al.*, Emerging applications of stimuli-responsive polymer materials, Nat. Mater. **9**, 101 (2010).

[20] A. Tripathi, Y. Ko, M. Kim, Y. Lee, S. Lee, J. Park, Y.-W. Kwon, J. Kwak, and H. Y. Woo, Optimization of thermoelectric properties of polymers by incorporating oligoethylene glycol side chains and sequential solution doping with preannealing treatment, Macromolecules **53**, 7063 (2020).

[21] W. Shi, Z. Shuai, and D. Wang, Tuning thermal transport in chain-oriented conducting polymers for enhanced thermoelectric efficiency: A computational study, Adv. Funct. Mater. **27**, 1702847 (2017).

[22] G.-H. Kim, D. Lee, A. Shanker, L. Shao, M. S. Kwon, D. Gidley, J. Kim, and K. P. Pipe, High thermal conductivity in

amorphous polymer blends by engineered interchain interactions, Nat. Mater. **14**, 295 (2015).

[23] G. W. Halek, Relationship between polymer structure and performance in food packaging applications, *Food and Packaging Interactions*, edited by Joseph H. Hotchkiss (ACS Publications, Washington DC, 1988), pp. 195–202.

[24] J. P. Jain, W. Y. Ayen, A. J. Domb, and N. Kumar, Biodegradable polymers in drug delivery, *Biodegradable Polymers in Clinical Use and Clinical Development*, edited by A. J. Domb, N. Kumar and A. Ezra (Wiley, New Jersey, 2011), pp. 1–58.

[25] G. Maier, Polymers for microelectronics, Mater. Today **4**, 22 (2001).

[26] M. J. Stevens, Interfacial fracture between highly cross-linked polymer networks and a solid surface: Effect of interfacial bond density, Macromolecules **34**, 2710 (2001).

[27] D. Mukherji and C. F. Abrams, Microvoid formation and strain hardening in highly cross-linked polymer networks, Phys. Rev. E **78**, 050801(R) (2008).

[28] G. Lv, B. Soman, N. Shan, C. M. Evans, and D. G. Cahill, Effect of linker length and temperature on the thermal conductivity of ethylene dynamic networks, ACS Macro Lett. **10**, 1088 (2021).

[29] S. R. White, N. R. Sottos, P. H. Geubelle, J. S. Moore, M. R. Kessler, S. Sriram, E. N. Brown, and S. Viswanathan, Autonomic healing of polymer composites, Nature (London) **409**, 794 (2001).

[30] M. Sharifi, C. Jang, C. Abrams, and G. Palmese, Toughened epoxy polymers via rearrangement of network topology, J. Mater. Chem. A **2**, 16071 (2014).

[31] B. Gold, C. Hövelmann, N. Lühmann, W. Pyckhout-Hintzen, A. Wischnewski, and D. Richter, The microscopic origin of the rheology in supramolecular entangled polymer networks, J. Rheol. **61**, 1211 (2017).

[32] M. Hess, E. Roeben, A. Habicht, S. Seiffert, and A. M. Schmidt, Local dynamics in supramolecular polymer networks probed by magnetic particle nanorheology, Soft Matter **15**, 842 (2019).

[33] Z. Rahil, S. Pedron, X. Wang, T. Ha, B. Harley, and D. Leckband, Nanoscale mechanics guides cellular decision making, Integrative Biol. **8**, 929 (2016).

[34] B. Persson and M. Scaraggi, Some comments on hydrogel and cartilage contact mechanics and friction, Tribol. Lett. **66**, 23 (2018).

[35] C. H. Mathis, R. Simič, C. Kang, S. N. Ramakrishna, L. Isa, and N. D. Spencer, Indenting polymer brushes of varying grafting density in a viscous fluid: A gradient approach to understanding fluid confinement, Polymer **169**, 115 (2019).

[36] R. Simič, C. H. Mathis, and N. D. Spencer, A two-step method for rate-dependent nano-indentation of hydrogels, Polymer **137**, 276 (2018).

[37] M. K. Singh, C. Kang, P. Ilg, R. Crockett, M. Kröger, and N. D. Spencer, Combined experimental and simulation studies of cross-linked polymer brushes under shear, Macromolecules **51**, 10174 (2018).

[38] M. H. Müser, H. Li, and R. Bennewitz, Modeling the contact mechanics of hydrogels, Lubricants **7**, 35 (2019).

[39] R. Akhtar, E. R. Draper, D. J. Adams, and J. Hay, Oscillatory nanoindentation of highly compliant hydrogels: A critical comparative analysis with rheometry, J. Mater. Res. **33**, 873 (2018).

[40] Z. I. Kalcioglu, R. Mahmoodian, Y. Hu, Z. Suo, and K. J. Van Vliet, From macro-to microscale poroelastic characterization

of polymeric hydrogels via indentation, Soft Matter **8**, 3393 (2012).

[41] S. Backes, P. Krause, W. Tabaka, M. U. Witt, and R. von Klitzing, Combined cononsolvency and temperature effects on adsorbed PNIPAM microgels, Langmuir **33**, 14269 (2017).

[42] J. N. M. Boots, D. W. te Brake, J. M. Clough, J. Tauber, J. Ruiz-Franco, T. E. Kodger, and J. van der Gucht, Quantifying bond rupture during indentation fracture of soft polymer networks using molecular mechanophores, Phys. Rev. Materials **6**, 025605 (2022).

[43] S. Mathesan, A. Rath, and P. Ghosh, Molecular mechanisms in deformation of cross-linked hydrogel nanocomposite, Mater. Sci. Eng. C **59**, 157 (2016).

[44] D. M. Ebenstein and L. A. Pruitt, Nanoindentation of biological materials, Nano Today **1**, 26 (2006).

[45] Y. M. Efremov, M. Velay-Lizancos, C. J. Weaver, A. I. Athamneh, P. D. Zavattieri, D. M. Suter, and A. Raman, Anisotropy vs isotropy in living cell indentation with AFM, Sci. Rep. **9**, 5757 (2019).

[46] V. A. Harmandaris, V. G. Mavrantzas, and D. N. Theodorou, Atomistic molecular dynamics simulation of stress relaxation upon cessation of steady-state uniaxial elongational flow, Macromolecules **33**, 8062 (2000).

[47] M. Kröger, C. Luap, and R. Muller, Polymer melts under uniaxial elongational flow: Stress- optical behavior from experiments and nonequilibrium molecular dynamics computer simulations, Macromolecules **30**, 526 (1997).

[48] T. Murashima, K. Hagita, and T. Kawakatsu, Viscosity overshoot in biaxial elongational flow: Coarse-grained molecular dynamics simulation of ring–linear polymer mixtures, Macromolecules **54**, 7210 (2021).

[49] J. M. Kim, R. Locker, and G. C. Rutledge, Plastic deformation of semicrystalline polyethylene under extension, compression, and shear using molecular dynamics simulation, Macromolecules **47**, 2515 (2014).

[50] T. Aoyagi and M. Doi, Molecular dynamics simulation of entangled polymers in shear flow, Comput. Theor. Polym. Sci. **10**, 317 (2000).

[51] D. Parisi, S. Costanzo, Y. Jeong, J. Ahn, T. Chang, D. Vlassopoulos, J. D. Halverson, K. Kremer, T. Ge, M. Rubinstein *et al.*, Nonlinear shear rheology of entangled polymer rings, Macromolecules **54**, 2811 (2021).

[52] J. Chen, J. Shi, Y. Wang, J. Sun, J. Han, K. Sun, and L. Fang, Nanoindentation and deformation behaviors of silicon covered with amorphous SiO_2: A molecular dynamic study, RSC Adv. **8**, 12597 (2018).

[53] S. Plimpton, Fast parallel algorithms for short-range molecular dynamics, J. Comput. Phys. **117**, 1 (1995).

[54] K. Kremer and G. S. Grest, Dynamics of entangled linear polymer melts: A molecular-dynamics simulation, J. Chem. Phys. **92**, 5057 (1990).

[55] T. Ge, F. Pierce, D. Perahia, G. S. Grest, and M. O. Robbins, Molecular Dynamics Simulations of Polymer Welding: Strength from Interfacial Entanglements, Phys. Rev. Lett. **110**, 098301 (2013).

[56] D. Mukherji and M. K. Singh, Tuning thermal transport in highly cross-linked polymers by bond-induced void engineering, Phys. Rev. Materials **5**, 025602 (2021).

[57] D. Mukherji and C. F. Abrams, Mechanical behavior of highly cross-linked polymer networks and its links

to microscopic structure, Phys. Rev. E **79**, 061802 (2009).

[58] M. L. Falk and J. S. Langer, Dynamics of viscoplastic deformation in amorphous solids, Phys. Rev. E **57**, 7192 (1998).

[59] K. M. Salerno and M. O. Robbins, Effect of inertia on sheared disordered solids: Critical scaling of avalanches in two and three dimensions, Phys. Rev. E **88**, 062206 (2013).

[60] M. Ozawa, L. Berthier, G. Biroli, A. Rosso, and G. Tarjus, Random critical point separates brittle and ductile yielding transitions in amorphous materials, Proc. Natl. Acad. Sci. USA **115**, 6656 (2018).

[61] C. Ruscher and J. Rottler, Avalanches in the athermal quasistatic limit of sheared amorphous solids: An atomistic perspective, Tribol. Lett. **69**, 64 (2021).

[62] W. C. Oliver and G. M. Pharr, Measurement of hardness and elastic modulus by instrumented indentation: Advances in understanding and refinements to methodology, J. Mater. Res. **19**, 3 (2004).

[63] M. Muthukumar, M. S. Bobji, and K. R. Y. Simha, Cone cracks in tissue-mimicking hydrogels during hypodermic needle insertion: The role of water content, Soft Matter **18**, 3521 (2022).

[64] R. S. Hoy and M. O. Robbins, Strain Hardening in Polymer Glasses: Limitations of Network Models, Phys. Rev. Lett. **99**, 117801 (2007).

[65] Y. Zhao, M. K. Singh, K. Kremer, R. Cortes-Huerto, and D. Mukherji, Why do elastin-like polypeptides possibly have different solvation behaviors in water–ethanol and water–urea mixtures? Macromolecules **53**, 2101 (2020).

[66] G. Lv, E. Jensen, C. Shen, K. Yang, C. M. Evans, and D. G. Cahill, Effect of amine hardener molecular structure on the thermal conductivity of epoxy resins, ACS Appl. Polymer Mater. **3**, 259 (2021).

Correction: An author contribution statement was missing and has been added after the Acknowledgments.

Second Correction: The parameter values provided below Eq. (3) were incorrect and have been fixed.